A Nature Portfolio journal



https://doi.org/10.1038/s43247-025-02883-0

Changing Northern Hemisphere weather linked to warming amplification in High Mountain Asia

Check for updates

Yongkun Xie ¹, Jianping Huang ¹, Guoxiong Wu^{2,3}, Jiaqin Mi ^{1,4}, Yimin Liu ^{2,3}, Zifan Su ⁵, Yuzhi Liu^{1,4} & Xiaodan Guan ^{1,4}

High Mountain Asia is a global warming hotspot, yet its influence on Northern Hemisphere extreme weather-related synoptic temperature variability remains unclear. Combining observations and numerical model simulations, we show that amplified High Mountain Asia warming has substantially enhanced summer synoptic temperature variability (>21%) in Canada and Russia while reducing winter variability (>19%) in Eastern Europe and the Nordic Seas during 1940–2022. These changes are primarily driven by altered high-frequency temperature advection. High Mountain Asia warming modifies horizontal temperature gradients, strengthening them in Canada and Russia in summer but weakening them in the Nordic Seas and Eastern Europe in winter. These patterns arise from hemispheric teleconnections that redistribute temperature and modulate atmospheric circulation stability via changes in jet streams, Rossby waves, and air-sea interactions. Our findings highlight High Mountain Asia warming's far-reaching impacts on Northern Hemisphere weather variability, extending beyond its well-known local climate effects.

High Mountain Asia (HMA), encompassing the Earth's Third Pole and the Asian Water Towers^{1,2}, represents one of the most remarkable topographical features on our planet. The role of HMA's topography in shaping both local and remote climates has been acknowledged for a long time³. In the context of paleoclimate evolution and contemporary climate variability, the mechanical and thermal forcing of HMA exerts a profound influence on the Asian climate⁴⁻⁸. Recent studies have further demonstrated that HMA's thermal forcing significantly impacts present-day climate variability worldwide through modulating large-scale atmospheric circulations and air-sea interactions⁹⁻¹¹.

HMA is experiencing accelerated warming under global warming^{2,12-14}. From 1979 to 2020, its annual warming rate was 1.8 times the global average¹⁵. This amplified warming in HMA has been proven to drive both local and remote climatic changes. For instance, it has contributed to increased South Asian monsoon precipitation¹⁶ and amplified Arctic warming¹⁷. However, while the effects on climate are well-studied, the influence of HMA warming on weather patterns in remote regions remains largely unexplored.

Compared to the flat Asian topography during the paleoclimate era, the uplift of HMA throughout its geological evolution has significantly reduced winter synoptic temperature variability (STV) across most of the Eurasian continent¹⁸. Unlike the well-documented changes in mean temperature characteristics (e.g., global warming), STV represents temperature variance features that directly reflect weather variability^{19,20}. This STV reduction suggests a decreased frequency and intensity of extreme cold winter events, resulting in relatively milder winter conditions that are more conducive to human habitation across Eurasia. Additionally, the uplift of HMA has had a differential impact on tropical cyclones: it significantly increased the frequency of tropical cyclones in the western North Pacific while simultaneously decreasing their occurrence in the Arabian Sea²¹. Consequently, the HMA uplift has exerted a notable influence on summer weather patterns associated with tropical cyclones.

Beyond the role of HMA uplift in the paleoclimate, ongoing warming in HMA has contributed to an upward trend in the number of tropical cyclones in the western North Pacific over recent decades²². Abnormal thermal forcing from HMA has been demonstrated to trigger the intensi-

fication of strong storms downstream of the Tibetan Plateau via diabatic and advective modifications in cyclogenesis and development ^{23,24}. Moreover, interannual variations in HMA thermal forcing, closely linked to changes in snow cover, have been hypothesized to modulate the interannual variability of Eurasian summer heatwaves²⁵. However, despite these established connections to tropical cyclones and Eurasian heatwaves, whether historical and current HMA warming has influenced the observed changes in weather patterns across the broader Northern Hemisphere remains an important and unresolved question.

To address this question, weather fluctuations were assessed using STV^{18-20,26}. Aligning with previous studies, STV was defined as the variance of high-frequency near-surface air temperature after band-pass filtering for 2 to 15 days^{18,26}, as defined in Eq. (1). Three-hourly data were used in this study to calculate STV. Figure 1a, c shows the climatological distribution of the STV across the Northern Hemisphere during boreal summer and winter for the 1940-2022 period based on ERA5 reanalysis data. Note that ERA5 data were used to represent the observed changes in STV because substantial missing values in the station-based observational dataset hamper the analysis of long-term climate change. The climatological STV generally shows larger values over the regions with stronger horizontal temperature gradients and higher circulation variabilities, such as over Ural blocking regions and storm track regions (Fig. 1), as also suggested by previous studies^{18,20,26-29}. In simple terms, when wind patterns are similar, stronger temperature contrasts between regions lead to bigger temperature swings as winds move air masses. On the other hand, if temperature contrasts stay the same, more variable winds cause stronger temperature fluctuations. In general, greater wave amplitudes in Rossby waves, more frequent blocking events, and cyclone/anticyclone occurrences produce higher atmospheric circulation variability.

Asian regions with elevations higher than 500 m are defined as HMA, which follows the benchmark experimental designs from Global Monsoons Model Intercomparison Project $(GMMIP)^{30}$ of the Coupled Model Intercomparison Project phase 6 $(CMIP6)^{31}$. The coupled Community Earth System Model (CESM), version 2.1.3, with 0.9×1.25 degree finite volume grid³², was used to perform numerical experiments. In the fully coupled

CESM model, the control run was the historical experiment (HIST) from 1850 to 2014, while the sensitivity run halved the sensible heat flux throughout the entire atmospheric column over HMA (HMA-sh0.5) at each time step of model integration. Monthly data were output for the period 1850–2014, while three-hourly data were output only for the last fifteen years (2000–2014) to save storage costs. Since this study focuses on STV derived from three-hourly data, we conducted three ensemble members for the 2000–2014 simulations (Table S1) to ensure robustness.

The model demonstrates good performance in simulating the climatology of key variables, despite some regional biases (Fig. S1). Specifically, it produces cooler summers and warmer winters over the extratropical continents compared to observations (Fig. S1c, f), and exhibits overestimated precipitation over East Asia in summer and the North Pacific in winter (Fig. S1i, l). The spatial pattern of simulated snow cover agrees well with the binary observational data, with visual differences attributable to the contrast between the model's continuous fractional values and the observed snow/no snow classification (Fig. S1m-r). It also captures the climatological patterns of STV across the Northern Hemisphere reasonably well, although some regional magnitude discrepancies exist (Fig. 1). Specifically, the HIST simulation shows stronger summer STV over Canada (Fig. 1a, b) but weaker winter STV over Eurasia (Fig. 1c, d) compared to observations. Beyond the control run, we evaluated the CESM's performance in sensitivity experiments. We conducted atmosphere-only historical (amip-HIST) and nosensible heat (amip-HMA-nosh) experiments to enable direct comparison with benchmark GMMIP results. The temperature and precipitation differences between amip-HIST and amip-HMA-nosh show high consistency between CESM and two GMMIP model simulations (Fig. S2). Taken together, these results demonstrate that CESM reliably reproduces both the climatological patterns and sensitivity responses crucial for our study.

The benchmark no-sensible heat (nosh) experiment from GMMIP produces a ~4 °C temperature anomaly over HMA (Fig. S2a, c, e), consistent with the paleoclimate variability range but substantially larger than observed current variability. We consequently adopted the half-sensible heat (sh0.5) experiment, yielding a more moderate ~1.5 °C anomaly over HMA (Fig. S3b) that better aligns with current climate variability ranges^{13–15}, i.e.,

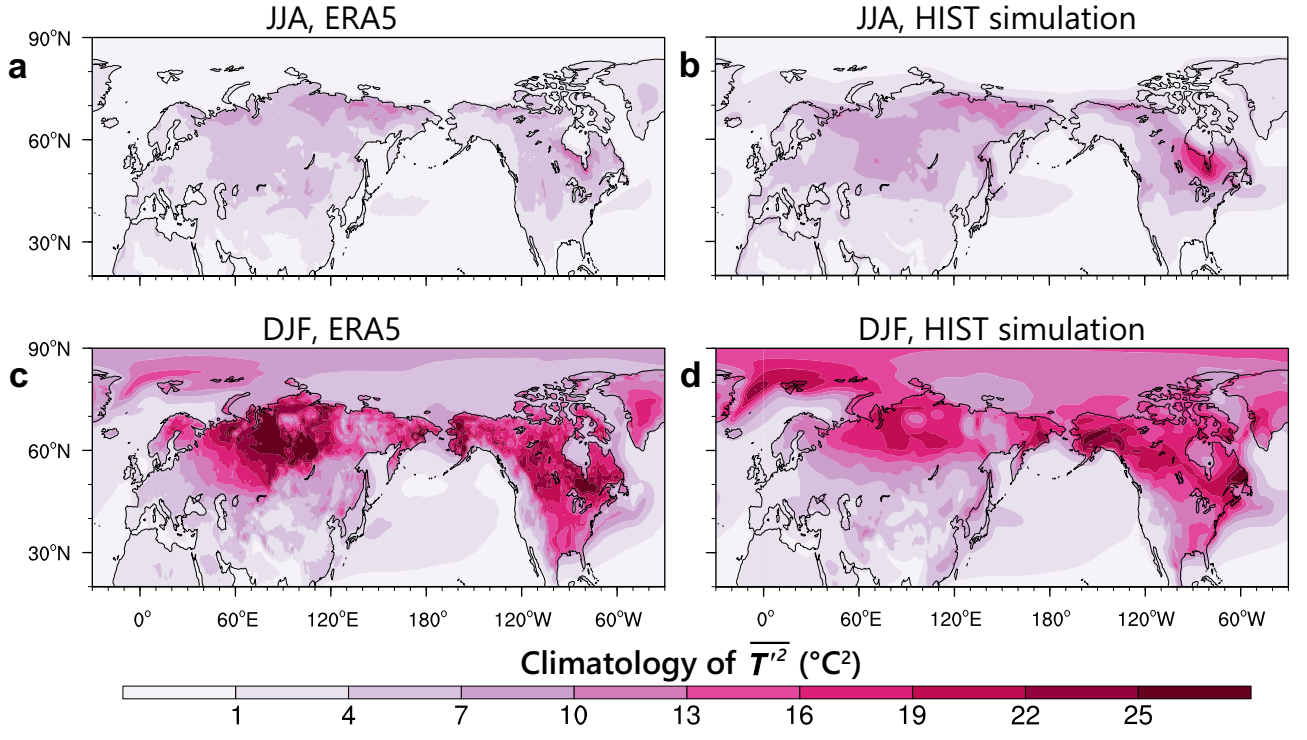


Fig. 1 | Climatological patterns of weather fluctuations. STV $(\overline{T'^2})$ averaged from 1940 to 2022 in (a) June to August (JJA) and (c) December to February (DJF), based on ERA5 reanalysis data. (b, d) Same as (a, c) but for the HIST experiment ensemble mean from 2000 to 2014.

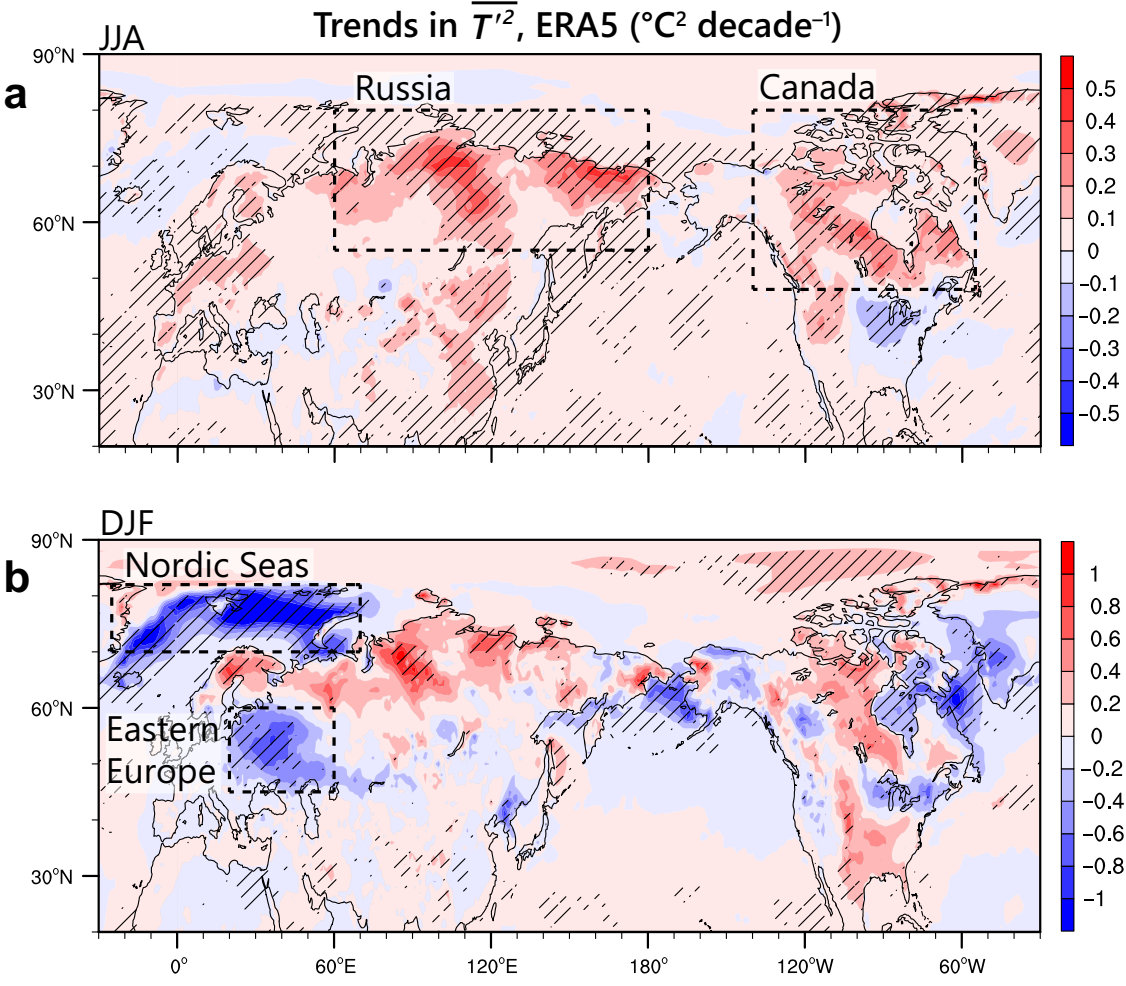


Fig. 2 | **Trends in weather fluctuations.** Linear trends in STV ($\overline{T'^2}$) for 1940–2022 in (**a**) JJA and (**b**) DJF, based on ERA5 data. The stripes indicate significant trends at the 95% ($P_{\rm adj}$ < 0.05) confidence level based on the two-tailed Student's t test and

false discovery rate (FDR)-adjusted P-values ($P_{\rm adj}$). Dashed rectangles highlight focus regions for analysis.

~2 °C/century HMA warming trend (Fig. S3a). Notably, both sh0.5 and nosh experiments dynamically adjust sensible heat flux at each model time step rather than prescribing a fixed forcing. This approach maintains complete feedback mechanisms, where sensible heat perturbations act primarily as a triggering factor for subsequent atmospheric adjustments. Compared to the control run^{9,30}, these sensitivity experiments ultimately produced a net cooling effect throughout the atmospheric column.

Since both observations and the HIST experiment inherently incorporate HMA warming effects, our sensitivity experiment (HMA-sh0.5) creates a cooler HMA condition with reduced thermal influence. The HIST minus HMA-sh0.5 differences thus isolate the specific impacts of HMA warming present in HIST. While alternative approaches involving sensible heat enhancement could theoretically reveal similar warming effects, our methodology adheres to the critical principle of keeping anomalies within realistic current climate ranges, which prevents unrealistic responses triggered by excessive forcing, e.g., paleoclimate-scale oceanic circulation changes³³. Furthermore, by scaling the differences between HIST and HMA-sh0.5 to match the observed magnitude of HMA warming from 1940 to 2022, the effects of HMA warming involved in observation can be estimated according to Eq. (2). This integrated framework—combining targeted sensitivity experiments with observationally constrained scalingeffectively disentangles HMA-induced climate signals from other forcing factors in the observational record.

This study focused on temperature variability rather than precipitation, which is another important component of weather. However, the impact of

precipitation-related latent heat release on temperature was included in the diabatic modification of temperature^{34,35}, as quantified using the thermodynamic equation³⁶. Unlike previous approaches that used pressure levels like 850 hPa to approximate surface conditions^{18,20,26}, we developed a model-level temperature tendency equation to directly diagnose the physical processes underlying STV from climate model output data^{29,37}. Through this method, numerical experiments, and observationally constrained scaling, we found that HMA warming substantially contributes to observed weather changes across many Northern Hemisphere regions for the 1940–2022 period, particularly in Russia, Canada, the Nordic Seas, and Eastern Europe.

Results

Observed trends in STV and the contribution of HMA warming

Considerable changes in STV were observed across the Northern Hemisphere from 1940 to 2022 (Fig. 2). During summer, statistically significant ($P_{\rm adj}$ < 0.05) positive STV trends occurred throughout most of the Northern Hemisphere, except for the eastern United States (Fig. 2a). The two most prominent positive STV trends in large-scale regions were found in Russia and Canada, indicating significantly increased synoptic-scale temperature fluctuations in these regions during summer.

In winter, both positive and negative STV trends were observed across the Northern Hemisphere (Fig. 2b). The two most prominent features were large-scale negative trends over the Nordic Seas and Eastern Europe, indicating significantly decreased synoptic-scale temperature fluctuations in these regions during winter. Climate model projections show continuing

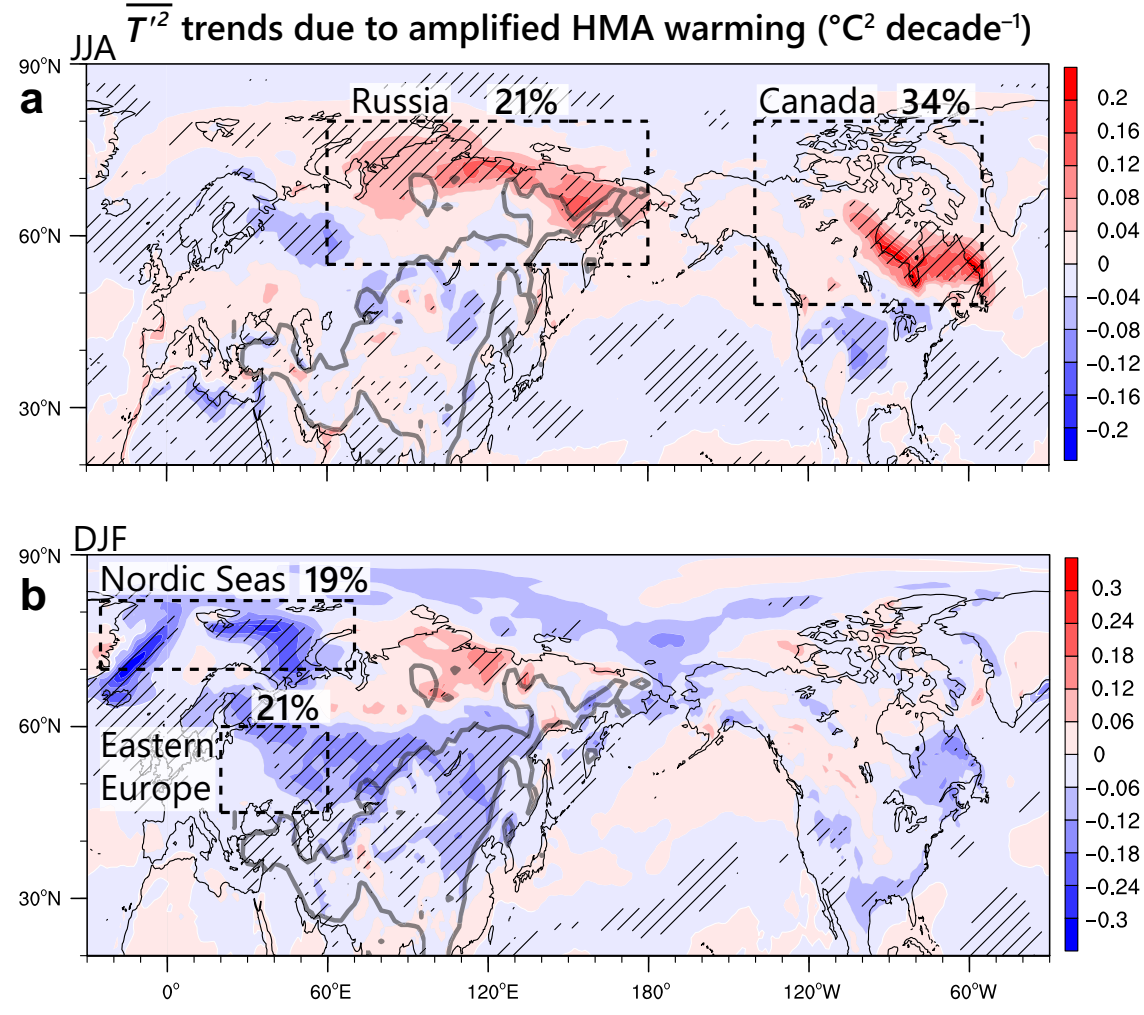


Fig. 3 | Amplified HMA warming-induced trends in STV. (a) JJA and (b) DJF STV (T'^2) trends attributable to amplified HMA warming for 1940–2022. Values represent ensemble means from numerical experiments (HIST minus HMA-sh0.5, Fig. S4) with observational scaling following Eq. (2). Striped areas indicate

statistically significant differences (P < 0.05, two-tailed Student's t test). Percentage values show the proportion of observed regional changes attributable to amplified HMA warming. The thick gray contour indicates 500 m elevation.

decreases in weather fluctuations over the Nordic Seas under both intermediate- and high-emission scenarios³⁸, with more pronounced decreases under high emissions. This suggests that reduced weather variability in the Nordic Seas may intensify with greater future warming. In addition, when sea ice melts and is replaced by open ocean, the greater heat capacity of water helps to stabilize temperatures, leading to reduced Arctic STV³⁸.

Based on CESM sensitivity experiments combined with observationally constrained scaling following Eq. (2), the potential contribution of HMA warming to observed trends in STV was isolated (Fig. 3). This scaling approach matches the modeled STV response to the actual observed strength of HMA warming. Specifically, the amplified component of HMA warming due to the regional feedback was quantified by comparing its temperature increase with the global mean warming rate (Fig. S3a, b). As detailed in the Introduction and Methods sections, the CESM model maintains all active feedbacks, where sensible heat serves only as a triggering factor while atmospheric and land surface feedbacks collectively determine the final HMA warming magnitude (HIST minus HMA-sh0.5). Consequently, the simulated sensible heat changes over HMA (Fig. S3c) do not perfectly correspond to the temperature changes (Fig. S3b). The simulated sensible heat changes exhibit pronounced increases over the Tibetan Plateau, particularly in its southern region (Fig. S3c). While some regional discrepancies exist between simulated and observed HMA temperature changes due to observational complexities and model limitations (Fig. S3a, b), the simulations successfully capture the large-scale impacts of HMA warming, as evidenced by positive changes in both temperature and sensible heat anomalies over the HMA (Fig. S3b, c).

Numerical experiments with observationally constrained scaling show that HMA warming significantly affects observed trends in STV across the four key regions (Fig. 3). In summer, HMA warming caused a significant STV increase in northern Russia, explaining 21% of the observed regional STV trends (Fig. 3a). It also enhanced STV in southeastern Canada, accounting for 34% of the regional STV trends. In winter, HMA warming significantly reduced STV in northeastern Eastern Europe, contributing 21% to the regional mean decrease (Fig. 3b). Across the Nordic Seas, HMA warming contributed 19% to reduced STV, with most pronounced effects in the Barents and Greenland Seas. Results are highly consistent across ensemble members. An exception is Eastern Europe in winter, where the contribution ratio varies in magnitude (7-43%; Fig. S5, which shows results from individual ensemble members). This is because STV changes there are dynamically controlled by high-frequency circulation variability (as discussed later), while other regions are thermodynamically dominated by horizontal temperature gradients. Dynamical factors exhibit greater intermodel variability³⁹, explaining this difference. According to the theory of mean temperature patterns controlling STV^{18,20,26,29}, most regional STV changes likely result from HMA warming-regulated temperature patterns. Overall, HMA warming impacts STV more strongly in downstream Canada

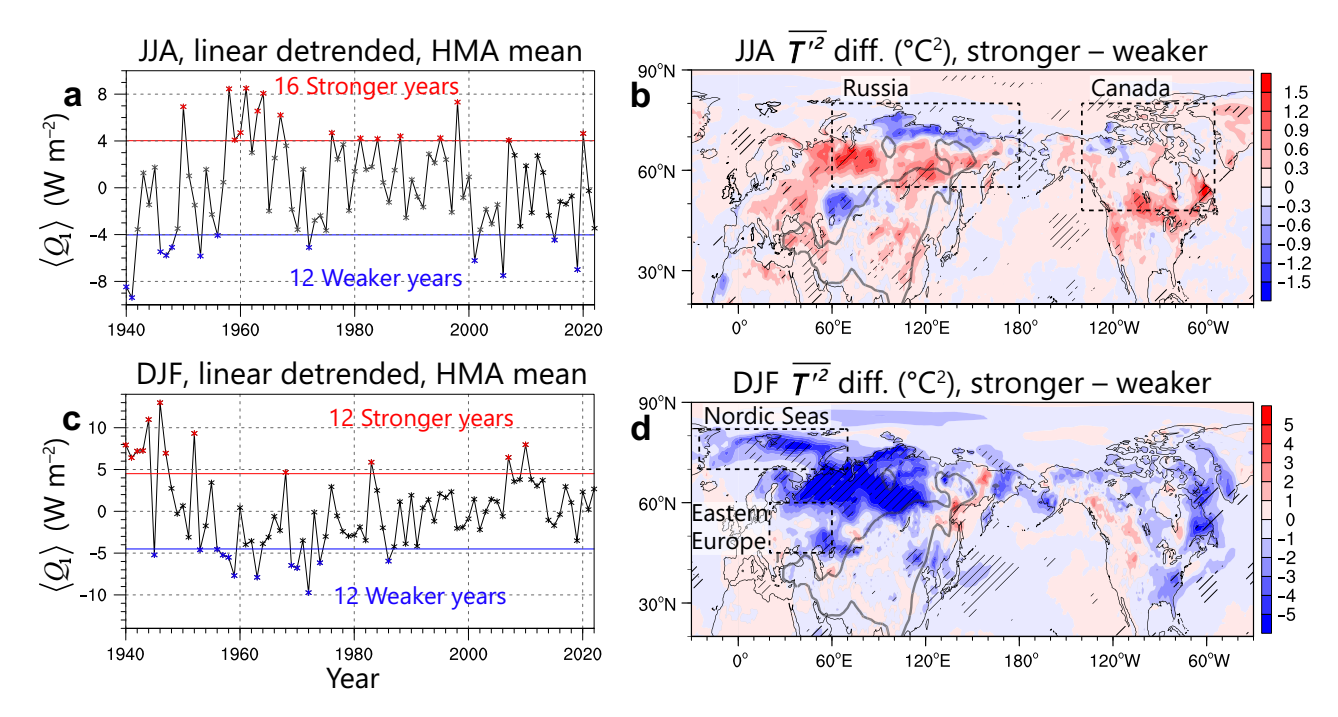


Fig. 4 | HMA warming-modulated interannual STV anomalies in observations. Time series of column-integrated atmospheric diabatic heating derived from the thermodynamic equation $\langle Q_1 \rangle$ in Eq. (7) averaged over the HMA from 1940 to 2022 in (a) JJA and (c) DJF, based on ERA5 data. Red and blue lines denote ± 1 standard

deviation, identifying years with stronger (above red line) and weaker (below blue line) HMA thermal forcing. (**b, d**) Corresponding STV $(\overline{T'^2})$ anomalies computed as differences between stronger and weaker forcing years. Striped regions indicate statistically significant differences (P < 0.05, two-tailed Student's t-test).

than other regions, primarily through its strong effects on Rossby waves along westerlies and jet streams^{3,8,11}, combined with oceanic repeater effects from the North Pacific and Atlantic Oceans by amplifying the downstream circulation and temperature changes⁹. These dynamical mechanisms will be detailed in a subsequent section.

Beyond long-term trend analysis combining simulations with observations, the HMA warming's impact on STV was further examined concerning variability spanning interannual to decadal timescales in observations. To avoid spurious correlations from linear trend components, we conducted composite analysis using linearly detrended variables. Consistent with the diabatic heating modifications in the numerical experiments, the HMA warming was quantified using atmospheric diabatic heating derived from the thermodynamic equation⁴⁰, as defined in Eq. (7), over the HMA region (Fig. 4a, c). This approach ensures direct comparability between observational composites and numerical simulations.

Compared to years with weaker thermal forcing, years with stronger HMA thermal forcing showed higher STV in Russia and Canada during summer (Fig. 4b) and lower STV in the Nordic Seas and Eastern Europe during winter (Fig. 4d). These composite analysis results generally agree with the HMA warming-induced positive and negative STV changes seen in long-term trends from numerical experiments (Fig. 3). However, the STV changes in the composite analysis show some regional-scale differences because this statistical method cannot fully separate the influence of HMA warming from other climate factors as precisely as controlled model experiments can. Collectively, both approaches consistently indicate that HMA warming contributes substantially to STV changes across all four regions, with relative contributions reaching at least 19%.

Physical processes underlying HMA warming impacts on remote STV

We developed a model-level temperature tendency equation²⁹, i.e., Eq. (4), to quantify the physical processes driving STV changes. By employing HIST minus HMA-sh0.5 differences in 2–15 day band-pass filtered temperature tendency variance derived from three-hourly data, we assessed each process's contribution to HMA warming-induced STV changes. These

processes, as defined in Eq. (8), include: adiabatic horizontal temperature advection (AD_h), adiabatic vertical motion-induced temperature modification (AD v), and diabatic heating from external energy sources (e.g., radiation and surface-atmosphere energy exchange; DIAB)^{29,36,37}. In simple terms, AD_h represents horizontal heat transport between regions, AD_v captures temperature changes caused by air moving up or down (which leads to expansion or compression), and DIAB includes local heating or cooling from radiation, clouds, and vertical energy transfer in the atmosphere. The climatological mean variance of the local temperature tendency (LOCAL; Fig. S6a, b), which quantifies the magnitude of synoptic-scale temperature change rates, shows spatial patterns consistent with STV distributions (Fig. 1). This confirms that our diagnostic approach, based on the variance of temperature tendencies, successfully captures the spatial characteristics of STV. Confirming previous findings 18,20,26, the AD_h term dominates large-scale STV patterns, while AD_v and DIAB show importance over topographic and coastal regions. The residual term's magnitude is three orders of magnitude smaller than the dominant terms (Fig. S6), further validating the methodological accuracy. Additional methodological details and comparative discussions are provided in the Methods section.

During summer, the AD_h (141%) and DIAB (105%) terms showed the strongest positive contributions to STV increase in Russia, each exceeding the AD_v contribution by at least threefold (Fig. 5a). Note that contributions can exceed 100% because positive and negative effects from different processes cancel each other out in the total calculation. Canada exhibited similar patterns, with AD_h and DIAB contributing 127% and 45%, respectively. However, covariance terms exerted negative influences: in Russia, Cov(AD_h, DIAB) (–161%) and Cov(AD_v, DIAB) (–30%); in Canada, Cov(AD_h, DIAB) alone accounted for –72% of STV modification. These results demonstrate that synoptic horizontal temperature advection and diabatic processes primarily drive increased weather variability in both regions, while their interactive effects offset these gains. Notably, the diabatic process plays a secondary role compared to horizontal advection, as further evidenced by spatial patterns (Fig. 5c).

During winter, both AD_h (138%) and AD_v (132%) terms contributed substantially to STV reduction in the Nordic Seas (Fig. 5b). In

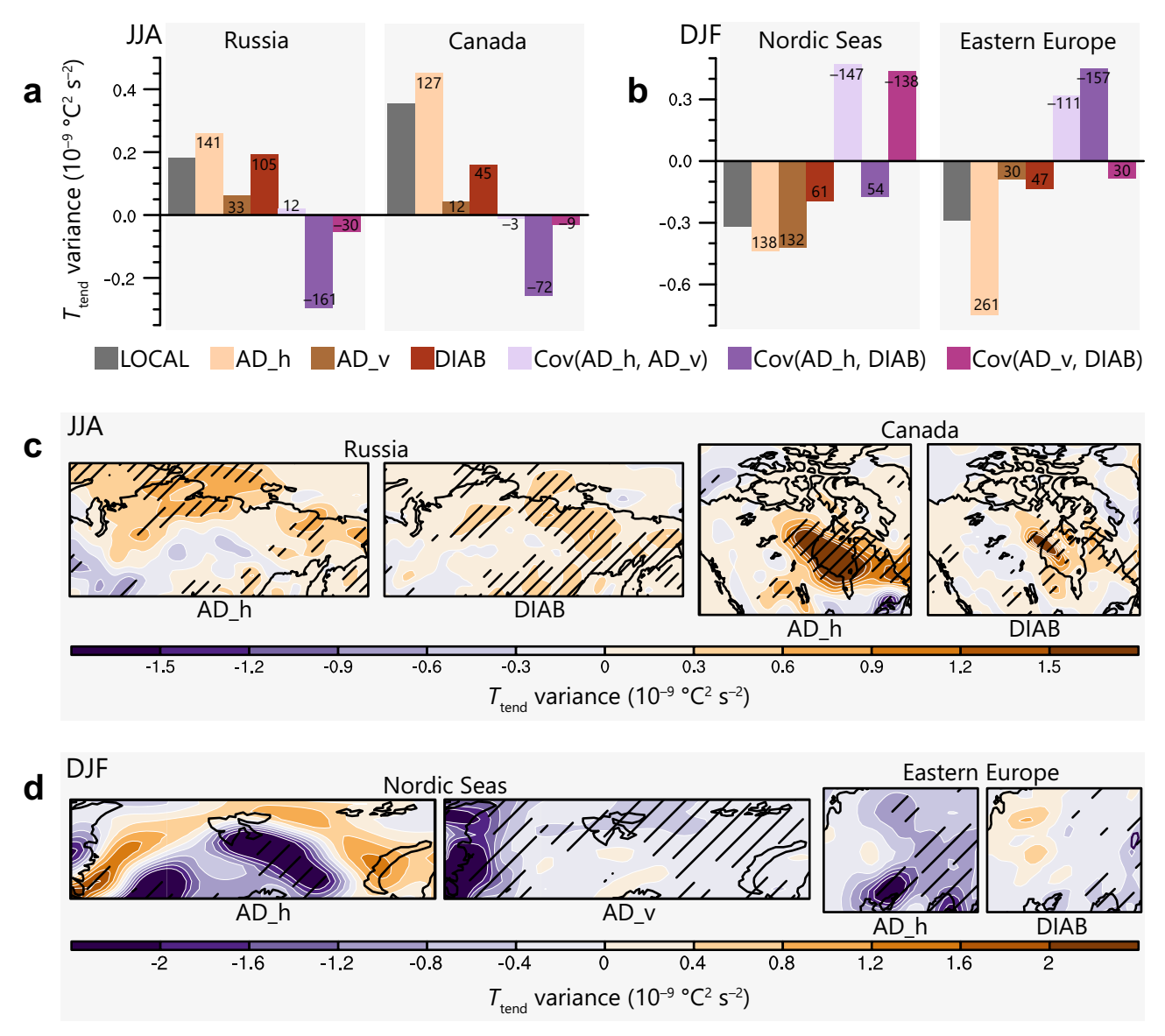


Fig. 5 | Physical process contributions to HMA warming-induced STV changes. a HMA warming-induced synoptic temperature tendency ($T_{\rm tend}$) variance changes (LOCAL) from: adiabatic horizontal temperature advection (AD_h), adiabatic vertical motion-induced temperature modification (AD_v), diabatic processes (DIAB), and their covariances (Cov), as defined in Eq. (8), averaged over two regions in JJA, based on ensemble means from numerical experiments (HIST minus HMA-

sh0.5) for 2000–2014. Numbers indicate each term's fractional contribution to LOCAL; values exceeding 100% occur due to offsetting positive and negative contributions, while the sum of all terms remains 100%. **b** Same as in (a) but for two regions in DJF. **c**, **d** Spatial patterns of the two dominant contributing terms to LOCAL. Striped regions indicate statistically significant differences (P < 0.05, two-tailed Student's t test).

Eastern Europe, AD_h dominated with a 261% contribution, significantly exceeding AD_v (30%) and DIAB (47%). Negative contributions arose from: Cov(AD_h, AD_v) and Cov(AD_v, DIAB) in the Nordic Seas, and Cov(AD_h, AD_v) and Cov(AD_h, DIAB) in Eastern Europe. Notably, while the regionally averaged Cov(AD_h, DIAB) showed net positive values, its spatial pattern (Fig. S7l) largely opposed the Nordic Seas STV changes (Fig. 3b), with positive contributions confined to northern margins. The AD_h spatial distribution closely matched Nordic Seas STV reductions, whereas AD_v effects were localized to western areas, likely from Greenland-induced vertical motion during wind fluctuations (Figs. 3b, 5d). Similarly, AD_h's dominance in Eastern Europe was evident in spatial patterns (Figs. 3b and S7d, f, h). These results demonstrate that synoptic horizontal temperature advection also primarily drives winter STV decreases in both regions.

Given the key role of horizontal temperature advection, the factors influencing it were investigated. Mathematically, horizontal temperature

advection depends on both wind patterns and temperature contrasts between regions. According to how synoptic variability is defined, the variance or an equivalent form of \overrightarrow{V} and $\nabla_h T$ should be examined. The eddy kinetic energy (EKE), as shown in Eq. (11), has a clear physical meaning and is a widely used factor in quantifying the high-frequency atmospheric circulation variability^{27,28}. Similarly, the strength of temperature contrasts between regions, as shown in Eq. (12), is measured by the norm of the horizontal temperature gradient and is widely recognized as a crucial factor in shaping synoptic-scale temperature variability^{18,20,26}. Taken together, the EKE and the norm of the horizontal temperature gradient are the dynamic and thermodynamic factors that determine the synoptic variability of horizontal temperature advection.

During summer, the enhanced horizontal temperature gradient in northern Russia and southeastern Canada (Fig. 6c) corresponded with increased AD_h contributions (Fig. 5c), while reduced EKE values (Fig. 6a) exhibited an inverse relationship with AD_h. In the Nordic Seas during

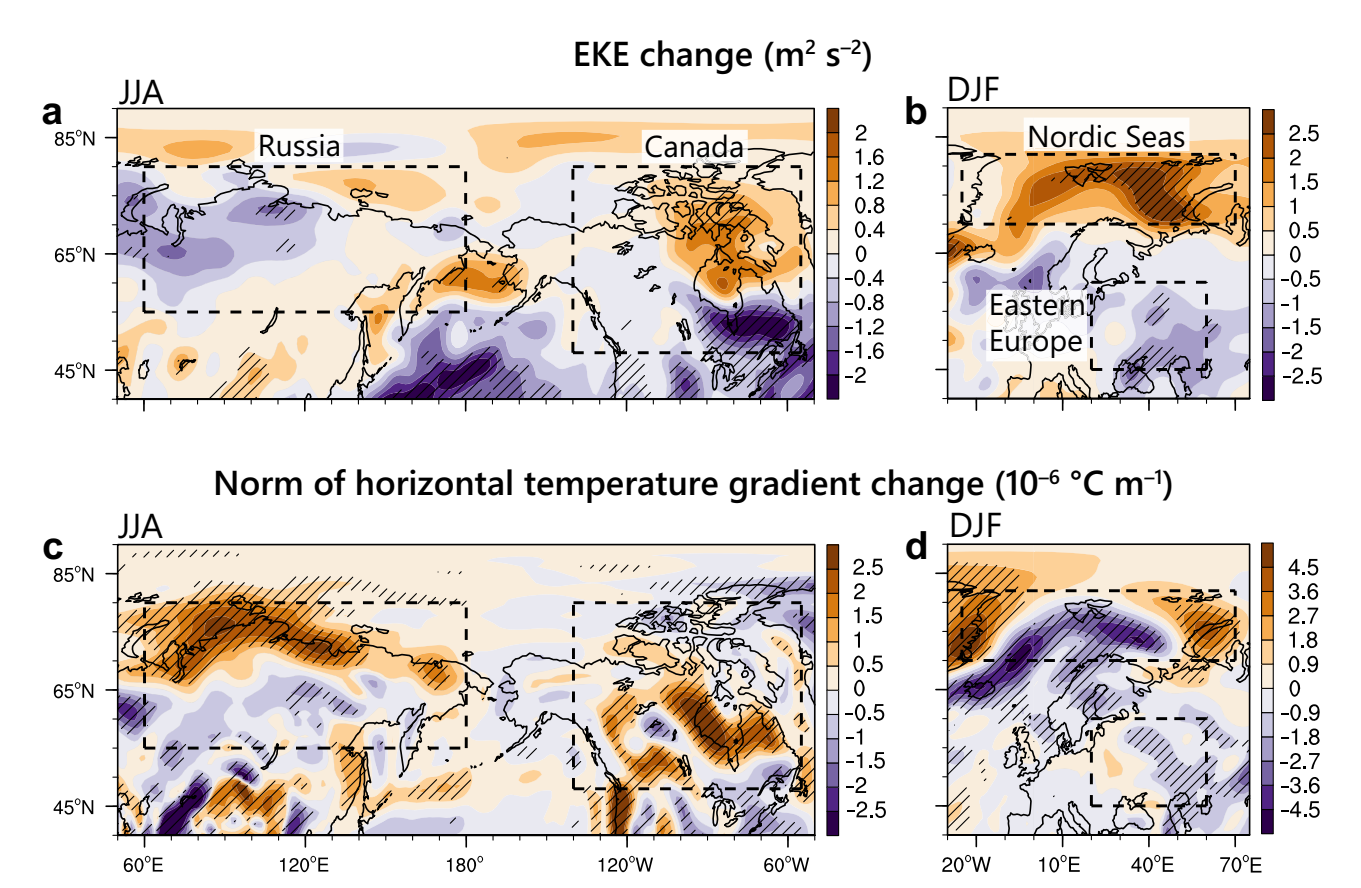


Fig. 6 | Key physical factors underlying HMA warming impacts on STV. a, b HMA warming-induced changes in eddy kinetic energy (EKE) according to Eq. (11) in JJA and DJF, respectively, derived from ensemble means of HIST minus

HMA-sh0.5 experiments for 2000–2014. Striped areas indicate statistically significant differences (P < 0.05, two-tailed Student's t test). **c**, **d** Same as (**a**, **b**) but for the norm of horizontal temperature gradient according to Eq. (12).

winter, the reduced horizontal temperature gradient (Fig. 6d) coincided with decreases in AD_h, while the elevated EKE (Fig. 6b) contrasted with AD_h (Fig. 5d). In Eastern Europe during winter, both EKE and the horizontal temperature gradient declined concurrently (Fig. 6b, d), with the spatial patterns of EKE showing a stronger correspondence to the reductions in AD_h (Fig. 5d). The simulation results are robust across ensemble members, with the exception of Eastern Europe in winter (Figs. S8 and S9, which show physical process contributions and key factors from individual ensemble members, respectively). In this region, the magnitude of the decrease in both EKE and the related AD_h varies considerably among members (Figs. S8b, d, f and S9b, f, j), mirroring the spread in STV changes seen in Fig. S5b, d, f. This coherence underscores the dominance of EKE in governing STV changes over winter Eastern Europe and attributes the intermodel spread primarily to dynamical processes. These modern climate relationships extend paleoclimatic evidence demonstrating HMA uplift's role in shaping EKE climatology and storm track evolution 18,28. Collectively, horizontal temperature gradients dominate STV changes in summer (Russia/Canada) and winter (Nordic Seas), whereas EKE variations primarily govern winter STV changes in Eastern Europe.

Hemispheric-scale teleconnection dynamics induced by amplified HMA warming

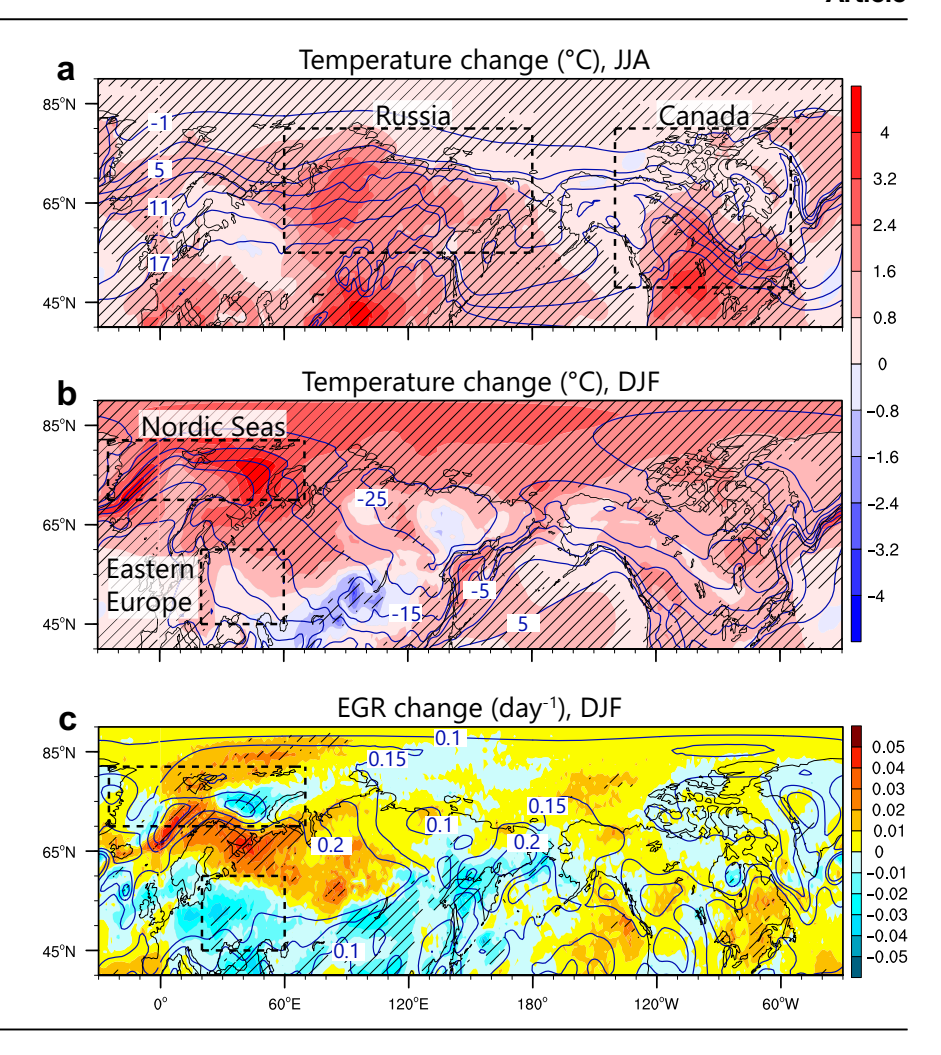
Given that horizontal temperature gradients and EKE are established as the two primary physical factors, the dynamics of HMA warming on STV can be attributed to teleconnections associated with these two variables. Horizontal temperature gradients are governed by spatial patterns of temperature changes, making the large-scale temperature change patterns induced by HMA warming fundamental. Previous studies have established that HMA warming affects remote temperature via modulating Rossby

waves, jet streams, and regional vertical circulation cells³⁻¹¹. In the midlatitudes, EKE depends on high-frequency atmospheric disturbances, which are ultimately driven by large-scale atmospheric instability. This type of instability is commonly measured using the maximum Eady growth rate (EGR)^{18,41}, as defined in Eq. (13). Therefore, we further examined temperature change patterns and EGR variations, as well as their overarching teleconnection dynamics.

Amplified HMA warming drives distinct seasonal temperature responses across Northern Hemisphere regions (Fig. 7). Summer features enhanced warming in southwestern Russia (Fig. 7a), intensifying horizontal temperature gradients along coastal regions by reinforcing land-sea thermal contrasts. The increased horizontal temperature gradients in Canada are also induced by enhanced warming in the south. Winter shows the strongest warming on poleward sides of the Barents and Greenland Seas (Fig. 7b), weakening background horizontal temperature gradients, while northwestern warming reduces gradients in southeastern Eastern Europe. The Eastern Europe EKE decrease is induced by diminished baroclinic instability (negative EGR changes; Fig. 7c), meaning a more stable atmosphere suppresses the formation of weather disturbances. Key changes induced by HMA warming are summarized as follows: summer's southern-enhanced warming amplifies Russian/Canadian horizontal temperature gradients; winter's northern-dominated warming reduces Nordic/Eastern European horizontal temperature gradients; and Eastern Europe EKE declines stem from enhanced atmospheric circulation stability.

Figure 8 demonstrates HMA warming-mediated large-scale circulation changes. During summer, HMA warming generates a belt of positive geopotential height anomalies in the upper troposphere. This anomalous high-pressure belt aligns with the climatological jet stream, creating circulation anomalies that weaken the westerlies to its south and enhance them to

Fig. 7 | HMA warming-induced changes in temperature and baroclinic instability. a, b Nearsurface air temperature differences in JJA and DJF, derived from ensemble means of HIST minus HMA-sh0.5 experiments for 2000–2014. Striped areas indicate statistically significant differences (P < 0.05, two-tailed Student's t test). Overlaid contours represent the climatological mean. c Same as (b) but for the maximum Eady growth rate (EGR), quantifying atmospheric baroclinic instability according to Eq. (13). Higher EGR values indicate a background state more favorable to the development of atmospheric eddies and thus higher EKE.



its north (Fig. 8a). This perturbed configuration promotes a poleward migration of the jet stream, consistent with established findings^{33,42}. However, these changes exhibit zonal asymmetry, with Russia experiencing the most pronounced northward displacement of high-pressure anomalies downstream of HMA (Fig. 8a). The wave activity flux (WAF) was employed to trace the pathways of Rossby wave propagation⁴³. Conceptually, the WAF represents the directional flow of energy within a Rossby wave packet, illustrating the trajectory along which the wave's energy propagates through the atmosphere. WAF reveals that Canada's summer high-pressure system results from prominent Rossby wave propagation along the jet stream waveguide originating from HMA. Winter patterns differ markedly, showing distinct Rossby wave signatures while demonstrating minor jet stream modifications (Fig. 8b). The primary winter influence manifests as a high-pressure anomaly affecting both the Nordic Seas and Eastern Europe, which is induced by the Rossby waves propagating via a circumglobal pathway along the jet stream according to WAF. Collectively, these patterns identify two key mechanisms: summer jet stream and Rossby wave anomalies connecting HMA warming to Russia and Canada; and winter circumglobal Rossby waves linking HMA to Nordic Seas and Eastern Europe.

Large-scale upper-level atmospheric circulations establish tele-connections between HMA and remote regions. Vertical coupling between lower- and upper-level circulations further links these atmospheric patterns with near-surface climate anomalies. During summer, HMA warming establishes a baroclinic structure characterized by low-level low pressure and upper-level high pressure (Fig. 8a, c). This system operates as a thermal air pump, driven by both sensible heating and other diabatic heating components, particularly latent heat release from precipitation 10,37. This

mechanism involves heating-induced rising air motions that create converging winds near the surface and diverging winds aloft, which subsequently trigger large-scale upper-level circulation anomalies. Away from HMA, these upper-level anomalies typically induce barotropic responses throughout the troposphere. Consequently, upper-level high pressure over Russia and Canada generates corresponding surface high-pressure systems (Fig. 8c), promoting subsidence in these regions (Fig. 8e). The resultant adiabatic heating and reduced cloud cover/precipitation from subsidence amplify regional warming. In winter, weaker convection and precipitationinduced latent heat release limit the generation of prominent local baroclinic responses by HMA warming. As a result, only a weak and shallow lowpressure system develops over the HMA (Fig. 8d). Nonetheless, the barotropic response in the remote region emerges, producing high pressure over both the Nordic Seas and Eastern Europe (Fig. 8d). This configuration fosters regional warming through subsidence (Fig. 8f) and enhances atmospheric stability in Eastern Europe. Although the Nordic Seas lie at the periphery of this high-pressure system, strong Arctic feedback mechanisms produce pronounced near-surface temperature responses, as discussed subsequently.

The mechanisms linking HMA warming with remote climatic impacts through atmospheric circulations and feedbacks are summarized in Fig. 9. Beyond these atmospheric processes, air-sea interactions play a pivotal role in mediating HMA's influence on Canada and the Nordic Seas. While Rossby waves naturally dissipate with distance, their propagation is partly sustained by jet streams acting as waveguides. In addition, the North Pacific Ocean acts as a critical oceanic repeater that amplifies the downstream impacts of HMA warming through positive feedbacks. Specifically, HMA warming enhances atmospheric humidity over the Pacific via large-scale

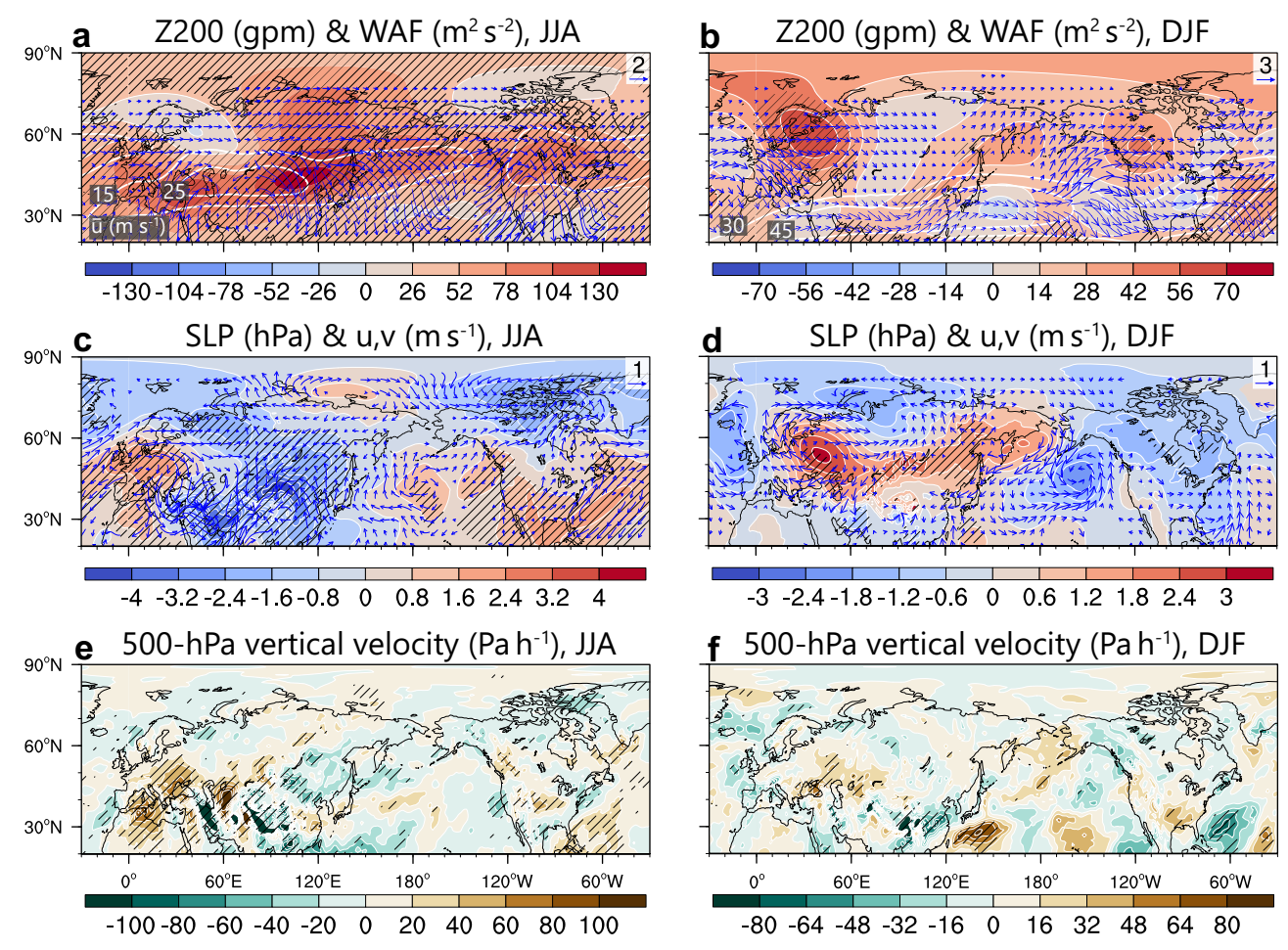


Fig. 8 | HMA warming-induced changes in large-scale atmospheric circulation. a, b Differences in 200-hPa geopotential height (Z200; shading) and wave activity flux (WAF; vectors) according to Eq. (14) in JJA and DJF, derived from ensemble means of HIST minus HMA-sh0.5 experiments for 2000–2014. The WAF shows the direction of Rossby wave propagation. Striped areas indicate statistically significant differences (P < 0.05, two-tailed Student's t test). Overlaid white contours indicate

climatological mean zonal wind (u). (c, d) Same as (a, b) but for sea level pressure (SLP; shading) and near-surface horizontal wind (u,v); vector). (e, f) Differences in vertical velocity at 500 hPa in JJA and DJF, derived from ensemble means of HIST minus HMA-sh0.5 experiments for 2000–2014. Striped areas indicate statistically significant differences (P < 0.05), two-tailed Student's t test).

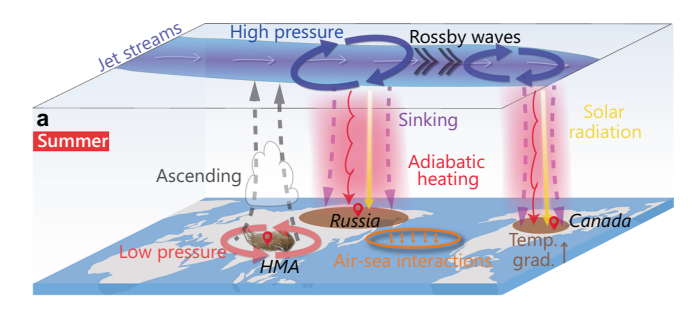
moisture transport. This process reduces the air-sea humidity contrast, thereby diminishing latent heat flux from the ocean. Concurrently, HMAinduced sinking motion reduces cloud cover, increasing shortwave radiation absorption. The resultant air-sea energy exchange further warms the ocean mixed layer, which in turn provides a feedback to the atmosphere particularly by sustaining Rossby wave propagation^{9,44}. This mechanism further elucidates why Canada exhibits the most pronounced climatic response to HMA warming. Similarly, HMA warming influences the Nordic Seas through Arctic air-sea interactions¹⁷. The HMA warminginduced anticyclonic anomalies over Nordic Seas/Eastern Europe (Fig. 8d) enhance poleward heat and moisture transport, activating feedback loops involving sea ice-albedo effects, radiation changes, and evaporation processes that collectively amplify Nordic Seas warming. Moreover, while the decline in snow cover (Fig. S10) contributes to regional warming in summer Russia/Canada and winter Eastern Europe (Fig. 7a, b), it is not the dominant factor because the spatial patterns of warming and snow loss do not match closely.

Discussion

This study demonstrates that HMA warming influences weather variability in remote regions—quantified by STV—primarily by modifying synoptic horizontal temperature advection, whereas diabatic processes play a secondary role. Nonetheless, diabatic processes can be crucial in individual extratropical weather systems⁴⁵, warranting further investigation into their

specific role in HMA's remote impacts on weather events. Two primary regimes changing synoptic temperature advection are identified: (1) driven by HMA-induced horizontal temperature gradients (dominant for summer Russia, Canada, and winter Nordic Seas), and (2) synoptic atmospheric circulation variability (dominant in winter Eastern Europe). Key regional responses include: (1) southern-enhanced warming over Russia/Canada strengthens horizontal temperature gradients and STV during summer, (2) northern-enhanced warming over Nordic Seas/Eastern Europe weakens horizontal temperature gradients and STV during winter, and (3) enhanced atmospheric circulation stability reduces synoptic circulation variability in Eastern Europe during winter. These findings align with established global temperature impacts of HMA warming^{8-11,16,17,42,46-48}, confirming the robustness of its remote effects on weather fluctuations.

HMA warming drives distinct seasonal teleconnection patterns through atmospheric pathways and air-sea interactions. Summer features a prominent baroclinic response over HMA, stimulating jet stream changes and Rossby wave propagation along the jet stream waveguide, generating high-pressure anomalies over Russia/Canada, while winter exhibits circumglobal Rossby waves establishing Nordic Seas/Eastern Europe high-pressure anomaly. These high-pressure systems induce regional warming through sinking motion-induced adiabatic heating and enhanced solar radiative heating across all four regions, while increasing atmospheric stability in winter Eastern Europe. As demonstrated by previous studies 9.17,44.46, air-sea interactions over the North Pacific and Arctic Oceans further



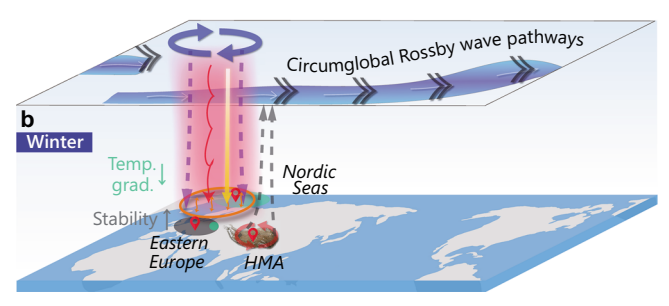


Fig. 9 | Schematic diagram of teleconnection mechanisms modulated by HMA warming. a, b HMA warming influences summer (Russia/Canada) and winter (Nordic Seas/Eastern Europe) climates through atmospheric circulations and feedbacks. HMA warming creates stronger low-level convergence and ascending motion via the thermal air pump mechanism (Fig. 8c-f), generating upper-level circulation anomalies that trigger: (1) summer Rossby wave trains downstream, forming high-pressure anomalies over Russia/Canada; and (2) winter circumglobal wave trains reaching upstream, producing Nordic Seas/Eastern Europe high pressure. For visual clarity, this figure schematically shows only the Rossby wave pathways and high-pressure anomalies that directly affect the target regions; detailed circulation patterns are provided in Fig. 8a, b. These high-pressure systems induce sinking motion (Fig. 8e, f), leading to adiabatic heating and solar radiative heating due to reduced cloud cover. The resultant regional warming patterns (Fig. 7a, b) and atmospheric stability changes over Eastern Europe (Fig. 7c) alter the horizontal temperature gradients and the EKE. Summer wave propagation is aided by North Pacific air-sea interactions9, while winter Nordic Seas warming is amplified by anticyclonic-driven poleward heat/moisture transport and air-sea feedbacks17.

amplify HMA warming's remote influence, particularly over Canada and the Nordic Seas. These mechanisms collectively explain the spatially heterogeneous yet robust remote impacts of HMA warming through vertically coupled atmospheric circulation changes and air-sea interactions.

These findings highlight the need to consider HMA warming when investigating weather in remote regions, particularly the four key areas identified. However, the majority of STV changes in each region should be attributed to regional warming patterns induced by external forcing and local feedbacks^{20,26,49}. HMA warming represents amplified regional heating exceeding anthropogenic emission-induced global averages⁴⁹, driven by both local feedbacks (snow/vegetation albedo, cloud-radiation, and water vapor effects)^{2,14–16} and remote oceanic forcing (Indian/Atlantic/Arctic influences)46,50,51. Beyond the isolated impact of long-term HMA warming examined in this study, the oceanic variability-mediated influence on weather variability at decadal timescales requires targeted investigation through expanded numerical experiments. Building on approaches like GMMIP's pacemaker experiments³⁰, future work should develop groups of pacemaker experiments to isolate HMA warming's remote oceanic drivers, thereby better understanding oceanic variability-mediated impacts on global weather.

While this study identifies HMA warming's influence on Northern Hemisphere weather, its effects have been inherently embedded in observed global climate change. However, accurately quantifying these impacts faces challenges due to: (1) sparse observations and complex topography introducing biases in observational/reanalysis data^{52–55}, and (2) model deficiencies in representing HMA climatology and climate changes, particularly

for snow cover and surface heat fluxes^{56,57}. These limitations highlight the critical need for improved observational networks and more physically realistic model parameterizations to reduce current uncertainties in assessing HMA warming's climatic role.

Methods

Data

The observational three-hourly and monthly near-surface air temperature data were from the European Centre for Medium-Range Weather Forecasting (ECMWF) reanalysis, version 5 (ERA5)⁵⁸, in a 1° × 1° grid. The three-hourly near-surface air temperature data were used to calculate the synoptic temperature variability (STV) according to Eq. (1). The monthly near-surface air temperature data were used to examine the seasonal mean temperature changes. The ERA5 three-hourly temperature, zonal and meridional wind velocity, vertical velocity in pressure coordinates, and surface pressure data in a 2° × 2° grid were used to calculate the diabatic heating of the atmosphere and its vertical column integration according to Eq. (7). ERA5 data are available from 1940 to the present, with the data utilized in this analysis being last updated in May 2023.

This study employs the Global Precipitation Climatology Project (GPCP) version 2.3 dataset. It has a spatial resolution of $2.5^{\circ} \times 2.5^{\circ}$ and a temporal coverage from January 1979 to the present. The dataset is accessible from the NOAA/OAR/ESRL PSL⁵⁹.

This study uses the National Oceanic and Atmospheric Administration (NOAA) Northern Hemisphere snow cover extent climate data record. The data are provided on a weekly basis on a 88×88 cell polar stereographic grid, covering the period from October 1966 to the present. The dataset is accessible from the NOAA National Centers for Environmental Information 60 .

Numerical experiments

The control and sensitivity runs for simulating the impact of HMA warming are HIST and HMA-sh0.5 experiments based on the fully coupled Community Earth System Model (CESM), version 2.1.3³². The atmosphere, land, and ocean components of the CESM model are CAM6, CLM5.0, and POP2, respectively, configured on a 0.9 × 1.25 degree finite volume grid (Table S1). The HIST experiment is a historical simulation from 1850 to 2014, which is identical to the historical experiment in the Coupled Model Intercomparison Project phase 6 (CMIP6)³¹, with external forcing such as greenhouse gas and aerosol emissions defined by the observed values. The HMA-sh0.5 experiment reduces the sensible heat flux (sh0.5) of the atmosphere over the HMA region by half, which creates a cooler atmosphere over HMA. As a result, the HIST minus HMA-sh0.5 difference reflects the impact of a warmer atmosphere over the HMA region. Monthly output data were generated for the entire simulation period (1850-2014), while three-hourly output was limited to the final 15 years (2000-2014) to save storage cost. Two additional ensemble runs were conducted for 2000-2014, initialized with conditions from 1998 and 1999, respectively (Table S1). This resulted in three complete ensemble runs for 2000-2014, all containing both three-hourly and monthly output data⁶¹.

The principles of experimental design for HMA-sh0.5 are outlined below. The large-scale topography affects climates through mechanical and thermal forcing 6.8. HMA thermal forcing changes with warming, thereby affecting the remote climate 7.16,17,22. Since sensible heat flux comprises the main component of atmospheric diabatic heating over the HMA 10,37, changes to sensible heat can substantially change the total diabatic heating. Therefore, numerical experiments widely use the sensible-heat-modification method to simulate the impact of HMA thermal forcing 6.9,11,30. Notably, sensible heat modification does not imply that only sensible heat changed while other components of diabatic heating remain unchanged. Modifying sensible heat flux acts as a triggering factor that sets off atmospheric adjustments, such as latent heat changes from precipitation changes, resulting in an overall diabatic heating change across the atmosphere over the HMA 6.17,37.

The technical details of the HMA-sh0.5 experiment are as follows. Two technical approaches are commonly utilized to modify the sensible heat over the HMA by manipulating different components of the coupled climate model. One approach modifies the land surface sensible heat flux exchanged between the land and atmosphere through the model coupler. The other approach modifies the sensible heat flux across the entire column of the atmosphere within the atmosphere component of the model. This study uses the latter, while the previous no-sensible-heat (nosh) experiment uses the former one^{30,46}. Furthermore, the sensible heat flux of the atmosphere is modified in each time step of model integration, thereby allowing for complete atmospheric adjustment and land-atmosphere feedbacks throughout the model execution. Due to the diffusive property of sensible heat transport and the active land-atmosphere feedbacks within the model, reducing either the land surface heat flux or the sensible heat flux of the atmosphere yields an equivalent effect in producing a cooler atmosphere over the HMA. Comparing CESM simulated results in this study with those from the Global Monsoons Model Inter-comparison Project (GMMIP)³⁰ reveals a high degree of consistency between the two approaches (Fig. S2), as elaborated below.

The GMMIP employs the atmosphere-only and no-sensible-heat experiment (amip-HMA-nosh) that is widely used in previous studies, wherein atmosphere-only experiments (abbreviated as amip following CMIP6 convention) are based on partly coupled models with prescribed sea surface temperature instead of an active ocean model³⁰. To verify our experimental designs and CESM performance, we also performed amip-HMA-nosh and amip-HIST experiments, wherein amip-HIST is the atmospheric-only historical experiment. Two models, i.e., FGOALS-f3-L and FIO-ESM-2-0, participated in GMMIP provided the results for amip-HMA-nosh and amip-HIST experiments. In line with HIST and HMAsh0.5 experiments, the amip-HIST minus amip-HMA-nosh difference reflects the impact of a warmer atmosphere over the HMA region. As shown in Fig. S2, the CESM-simulated temperature and precipitation changes are highly consistent with that of the two GMMIP models, which indicates the consistent effects of the aforementioned two approaches in modifying sensible heat over the HMA. As detailed in the introduction, totally removing the sensible heat generates a forcing that is much stronger than the current climate variability over the HMA. Therefore, HMA-sh0.5 with half sensible heat modification was employed in this study.

Synoptic temperature variability

STV is defined as the high-frequency temperature variance after band-pass frequency filtering at the synoptic timescale^{18,26,28}, which in this study is 2 to 15 days, as formulated in Eq. (1):

$$\overline{T^{\prime 2}} = \frac{1}{n} \sum_{i=1}^{n} (T_i - \bar{T})^2, \tag{1}$$

where T_i and \bar{T} indicate the temperature at each time point in a month and the monthly average, respectively, based on the three-hourly data after 2-to-15-day band-pass filtering.

To compare the results of the sensitivity experiment with observations, the differences in STV from the experiments should be scaled to the observed HMA warming trend (T_{trend}^{HMA} , Fig. S3a). This scaling is based on the sensitivity of the response to forcing, specifically the STV change (T_{diff}^{Y}) in response to the HMA temperature change (T_{diff}^{HMA} ; HMA regional average; Fig. S3b) in the HMA-sh0.5 experiment, as illustrated in Eq. (2). Since the amplified HMA warming relative to the global average indicates unique forcing from HMA, the global mean warming values (T_{trend}^{Globe} , global average) must be excluded when quantifying the effect of HMA warming (T_{trend}^{HMA} ;HMA regional average). Previous studies have proposed that the forcing of HMA warming has a cross-seasonal impact on the climate response HMA warming has a cross-seasonal impact on the climate response TMA warming has a cross-seasonal impact on the climate response TMA warming has a cross-seasonal impact on the climate response TMA warming has a cross-seasonal impact on the climate response TMA warming has a cross-seasonal impact on the climate response TMA warming has a cross-seasonal impact on the climate response TMA warming has a cross-seasonal impact on the climate response TMA warming has a cross-seasonal impact on the climate response TMA warming has a cross-seasonal impact on the climate response TMA warming has a cross-seasonal impact on the climate response TMA warming has a cross-seasonal impact on the climate response TMA warming has a cross-seasonal impact on the climate response TMA warming has a cross-seasonal impact on the climate response TMA warming has a cross-seasonal impact on the climate response TMA warming has a cross-seasonal impact on the climate response TMA warming the thread TMA warmin

response-to-forcing ratio $(\overline{T'^2}_{diff}/T_{diff}^{HMA})$ and the observed changes in forcing $(T_{trend}^{HMA}-T_{trend}^{Globe})$:

$$\overline{T'^{2}}_{HMA} = (T_{trend}^{HMA} - T_{trend}^{Globe}) \times \frac{\overline{T'^{2}}_{diff}}{T_{diff}^{HMA}},$$
 (2)

where T_{trend} indicates the observed temperature trend, while T_{diff} indicates the simulated temperature difference using HIST minus HMA-sh0.5.

Equation of physical processes underlying STV change

The temperature tendency equation, also known as the thermodynamic equation for temperature, in the pressure coordinate is as follows³⁶:

$$\frac{\partial T}{\partial t} = -\overrightarrow{V} \cdot \nabla_h T + \left(\frac{\kappa T}{p}\omega - \frac{\partial T}{\partial p}\omega\right) + \left(\frac{p}{p_0}\right)^{\kappa} \frac{d\theta}{dt},\tag{3}$$

where \overrightarrow{V} , ω , p, and $\theta = T(p_0/p)^\kappa$ indicate horizontal wind velocity, vertical velocity in units of Pa s⁻¹, pressure, and potential temperature, respectively. The two constants are $\kappa = 0.286$ and $p_0 = 100000$ Pa. Symbol ∇_h represents the horizontal gradient operator. As also described by Röthlisberger and Papritz³⁶, the left-hand side term represents the local temperature tendency, while the three right-hand side terms represent the temperature tendencies induced by adiabatic horizontal temperature advection, adiabatic vertical displacement of air and temperature convection, and diabatic heating due to external energy sources, respectively. To trace the evolution of temperature extremes, Röthlisberger and Papritz further derived the Lagrangian temperature-anomaly tendency equation along the backward trajectory of the air parcel. In contrast to Röthlisberger and Papritz's Lagrangian tracing method³⁶, the terrain-following form of Eq. (3), i.e., Eq. (4), provides a simpler approach to diagnose the physical processes leading to near-surface temperature changes from an Eulerian perspective that focuses on fixed points in space.

The temperature tendency equation in model-level coordinates is as follows, according to the vertical coordinate transformation rules:

$$\frac{\partial T}{\partial t} = -\overrightarrow{V} \cdot \nabla_h T + \left(\frac{\kappa T}{p}\omega - \frac{\partial T}{\partial p}\omega_{ml}\right) + \left(\frac{p}{p_0}\right)^{\kappa} \frac{d\theta}{dt}, \tag{4}$$

where ω_{ml} is the vertical velocity transformed from pressure-level coordinate to model-level coordinate 29,37 , and in the form of

$$\omega_{ml} = \omega - \frac{\partial p}{\partial t} - \overrightarrow{V} \cdot \nabla_h p. \tag{5}$$

Correspondingly, the diabatic heating of the atmosphere after vertical coordinate transformation is in the form of

$$\frac{d\theta}{dt} = \frac{\partial\theta}{\partial t} + \overrightarrow{V} \cdot \nabla_h \theta + \omega_{ml} \frac{\partial\theta}{\partial \rho}.$$
 (6)

Another form of diabatic heating is the often-used apparent heating $Q_1 = c_p (\frac{p}{p_0})^\kappa \frac{d\theta^{62}}{\partial t}$. The vertical integration of Q_1 across the atmosphere column⁴⁰ is used to quantify the thermal forcing of the HMA in observations, in the form of

$$\langle Q_1 \rangle = \int_{z_S}^{z_T} \rho Q_1 \, \mathrm{d}z = -\frac{1}{g} \int_{p_S}^{p_T} Q_1 \, \mathrm{d}p, \tag{7}$$

where p_S and $p_T = 200$ hPa indicate the surface and top pressures of the integration. Symbol g indicates the magnitude of gravity.

Subsequently, there are two approaches for quantifying the contributions of various physical processes to changes in STV. *Approach I* is to determine the high-frequency variance of Eq. (4) after 2-to-15-day band-

pass filtering, that is

$$\underbrace{\sigma^{2}\left[\frac{\partial T}{\partial t}\right]}_{\text{LOCAL}} = \underbrace{\sigma^{2}\left[-\overrightarrow{V}\cdot\nabla_{h}T\right]}_{\text{AD_h}} + \underbrace{\sigma^{2}\left[\frac{\kappa T}{p}\omega - \frac{\partial T}{\partial p}\omega_{ml}\right]}_{\text{AD_v}} + \underbrace{\sigma^{2}\left[\left(\frac{p}{p_{0}}\right)^{\kappa}\frac{d\theta}{dt}\right]}_{\text{DIAB}} + \underbrace{2\sigma\left[-\overrightarrow{V}\cdot\nabla_{h}T, \frac{\kappa T}{p}\omega - \frac{\partial T}{\partial p}\omega_{ml}\right]}_{\text{Cov}(AD_h, AD_v)} + \underbrace{2\sigma\left[-\overrightarrow{V}\cdot\nabla_{h}T, \left(\frac{p}{p_{0}}\right)^{\kappa}\frac{d\theta}{dt}\right]}_{\text{Cov}(AD_h, DIAB)} + \underbrace{2\sigma\left[\frac{\kappa T}{p}\omega - \frac{\partial T}{\partial p}\omega_{ml}, \left(\frac{p}{p_{0}}\right)^{\kappa}\frac{d\theta}{dt}\right]}_{\text{Cov}(AD_v, DIAB)} + \text{residual}$$

$$(8)$$

where σ^2 and σ represent the variance and covariance operators. The left-hand side term indicates the local STV change (LOCAL), while the six right-hand terms indicate the relative contributions of adiabatic horizontal temperature advection (AD_h), adiabatic vertical motion-induced temperature modification (AD_v) including vertical displacement of air and temperature convection, diabatic heating due to external energy sources such as radiation and surface-air energy exchange (DIAB), and the covariance of the three physical processes (Cov), respectively. The residual term represents the numerical error resulting from the finite difference.

term represents the numerical error resulting from the finite difference. Alternatively, *Approach II* is to determine the equation of variable $\frac{\partial T^2}{\partial t}$, as illustrated in Eq. (10)²⁹. The deductions are as follows: Introducing $T=\bar{T}+T'$ to the left-hand side of Eq. (4) and subtracting the monthly mean of Eq. (4) from it yield

$$\frac{\partial T'}{\partial t} = -\overrightarrow{V} \cdot \nabla_h T + \left(\frac{\kappa T}{p}\omega - \frac{\partial T}{\partial p}\omega_{ml}\right) + \left(\frac{p}{p_0}\right)^{\kappa} \frac{d\theta}{dt} \\
- \left[-\overrightarrow{\overrightarrow{V}} \cdot \nabla_h T + \left(\frac{\kappa T}{p}\omega - \overline{\frac{\partial T}{\partial p}}\omega_{ml}\right) + \left(\frac{p}{p_0}\right)^{\kappa} \frac{d\theta}{dt}\right].$$
(9)

Multiplying Eq. (9) by 2T', introducing $\frac{\overline{\partial T'^2}}{\partial t} = \overline{2T'\frac{\partial T'}{\partial t}}$, and applying the monthly mean to it yield

$$\frac{\overline{\partial T'^2}}{\partial t} = -\overline{2T' \cdot \overrightarrow{V} \cdot \nabla_h T} + \overline{2T' \cdot \left(\frac{\kappa T}{p}\omega - \frac{\partial T}{\partial p}\omega_{ml}\right)} + \overline{2T' \cdot \left(\frac{p}{p_0}\right)^{\kappa} \frac{d\theta}{dt}}.$$
(10)

Although Approach II appears more plausible and rigorous in mathematics, Approach I was implemented in this study because Approach II did not work in our case. The primary issue with Approach II lies in $\frac{\partial T^2}{\partial t} \neq \frac{\partial T'^2}{\partial t}$, in particular, the differing sequence of the averaging operation and the partial derivative between the two terms. The left-hand term calculates the tendency of T'^2 at each time point and then performs the averaging. In contrast, the right-hand term first calculates the average, which represents the STV in this study, and then performs the partial derivative. The right-hand term aligns with our objective to examine STV changes, whereas the left-hand term does not. Given the nonlinearity of the partial derivative, the different sequence of operations yields different results. Consequently, the left-hand term mathematically and statistically fails to adequately capture STV changes, as clearly illustrated by the following thought experiment about synoptic temperature evolution.

Weather events are characterized by waves of temperature anomalies that come and go. For example, if the temperature rises and then returns to normal after a week, it could result in $T_0'=0,2,4,6,4,2,0$ K for seven days consecutively. Similarly, for another case with greater synoptic temperature variability, it could be $T_1'=0,5,10,15,10,5,0$ K. The relevant variables are $T_0'^2=0,4,16,36,16,4,0$ K², $T_1'^2=0,25,100,225,100,25,0$ K², $\frac{\partial T_0'}{\partial t}=2,2,2,-2,-2,-2$, -2, -2 K d $^{-1}$, $\frac{\partial T_1'}{\partial t}=5,5,5,-5,-5,-5,-5$ K d $^{-1}$, $\frac{\partial T_0'^2}{\partial t}=4$, 12,20,-20,-12,-4 K² d $^{-1}$, $\frac{\partial T_1'^2}{\partial t}=25,75,125,-125,-75,-25$ K² d $^{-1}$, $\sigma^2[\frac{\partial T_0'}{\partial t}]=4$ K² d $^{-2}$, and $\sigma^2[\frac{\partial T_1'}{\partial t}]=25$ K² d $^{-2}$. As a result, $\frac{\partial T_0'}{\partial t}=0$ K d $^{-1}$, $\frac{\partial T_1'}{\partial t}=0$ K d $^{-1}$, $\frac{\partial T_1'}{\partial t}=0$ K d $^{-1}$, $\frac{\partial T_1'}{\partial t}=0$ K² d $^{-1}$, and $\frac{\partial T_1'}{\partial t}=0$ K² d $^{-1}$.

Obviously, the result $\frac{\overline{\partial T_1'^2}}{\partial t} = 0$ indicates that Approach II based on Eq. (10) is unable to detect the increased STV from T_0' to T_1' . In contrast, the result $\sigma^2[\frac{\overline{\partial T_0'}}{\partial t}] - \sigma^2[\frac{\overline{\partial T_0'}}{\partial t}] = 21$ demonstrates that Approach I based on Eq. (8) is effective.

The variance of the horizontal temperature advection term (AD_h) in Eq. (8) is jointly determined by the dynamical factor, that is, synoptic atmospheric circulation variability represented by the eddy kinetic energy (EKE)²⁷ with 2-to-15-day band-pass filtering, and the thermodynamic factor, represented by the norm of the horizontal temperature gradient $(|\nabla_h \bar{T}|)^{26}$, as follows:

$$EKE = (\overline{u'^2} + \overline{v'^2})/2, \tag{11}$$

$$|\nabla_h \bar{T}| = \sqrt{\left(\frac{\partial \bar{T}}{\partial x}\right)^2 + \left(\frac{\partial \bar{T}}{\partial y}\right)^2}.$$
 (12)

EKE is mathematically similar to turbulent kinetic energy⁶³, but it excludes the vertical velocity component. Turbulent kinetic energy is primarily used to describe small-scale turbulence within the atmospheric boundary layer, whereas EKE is applied to characterize large-scale atmospheric circulations. Both EKE and the norm of the horizontal temperature gradient have been widely recognized as key factors in examining the synoptic variability of horizontal temperature advection 18,20,26. EKE is determined by large-scale atmospheric circulation instability, usually quantified as maximum Eady growth rate (EGR)⁴¹—a metric directly explaining EKE's variations; higher EGR strengthens baroclinic instability, amplifies wind perturbations (u', v' in Eq. (11)), and boosts EKE (lower EGR has the opposite effect), thus making EGR a driver of EKE variability that links circulation instability to synoptic eddy energy. EGR is defined as follows:

$$EGR = 0.31 \frac{f}{N} \left| \frac{\partial u}{\partial z} \right|$$
 (13)

where where f and N are the Coriolis parameter and Brunt-Väisälä frequency, respectively.

Wave activity flux

The wave activity flux (WAF) represents the direction in which stationary wave trains propagate, namely the group velocity of a Rossby wave packet. This study utilizes the formulation of WAF as suggested by Takaya and Nakamura ⁴³, as follows:

$$\overrightarrow{WAF} = \frac{p \cos \phi}{2|\overrightarrow{\overrightarrow{V}}|} \begin{pmatrix} \frac{\overline{u}}{a^2 \cos^2 \phi} \left[\left(\frac{\partial \psi'}{\partial \lambda} \right)^2 - \psi' \frac{\partial^2 \psi}{\partial \lambda^2} \right] + \frac{\overline{v}}{a^2 \cos \phi} \left[\frac{\partial \psi'}{\partial \lambda} \frac{\partial \psi'}{\partial \phi} - \psi' \frac{\partial^2 \psi'}{\partial \lambda \partial \phi} \right] \\ \frac{\overline{u}}{a^2 \cos \phi} \left[\frac{\partial \psi'}{\partial \lambda} \frac{\partial \psi'}{\partial \phi} - \psi' \frac{\partial^2 \psi'}{\partial \lambda \partial \phi} \right] + \frac{\overline{v}}{a^2} \left[\left(\frac{\partial \psi}{\partial \phi} \right)^2 - \psi' \frac{\partial^2 \psi'}{\partial \phi^2} \right] \end{pmatrix}$$
(14)

where a indicates Earth's radius, ϕ and λ indicate latitude and longitude, respectively. ψ' indicates stream function anomaly with respect to the climatological mean.

Statistical methods

Linear trends were calculated using the least-squares linear regression approach, based on the NCAR Command Language (NCL)⁶⁴, as described at https://www.ncl.ucar.edu/Document/Functions/Contributed/regline_stats. shtml. The corresponding significances were estimated using two-tailed Student's *t* test. Since we examined the linear trends spatially, the P-values for the significance tests were adjusted according to the false discovery rate

(FDR) concept⁶⁵. The FDR-adjusted P-values were calculated as follows:

$$P_{\text{adj}} = P \times \frac{N}{\text{Rank}(P)},\tag{15}$$

where N represents the total number of grids north of 10° N in this study, and Rank(P) represents the rank of all P-values sorted in ascending order. The statistical significance level in this study was set at 95% ($P_{\rm adi}$ < 0.05).

The two-tailed Student's t-test was also used to determine the statistical significance (95% confidence level, P < 0.05) of the difference between the control (HIST) and sensitivity (HMA-sh0.5) runs, as described at https://www.ncl.ucar.edu/Document/Functions/Built-in/ttest.shtml.

The band-pass filtering based on Lanczos filtering method⁶⁶ was used to extract the synoptic variability components of the time series, as described at https://www.ncl.ucar.edu/Document/Functions/Built-in/filwgts_lanczos.shtml. The frequency band of synoptic variability^{18,26} ranges from 2 to 15 days in this study.

Reporting summary

Further information on research design is available in the Nature Portfolio Reporting Summary linked to this article.

Data availability

ERA5 hourly data at the near-surface are available at https://cds.climate.copernicus.eu/datasets/reanalysis-era5-single-levels?tab=overview.

ERA5 monthly data at the near-surface are available at https://cds.climate.copernicus.eu/datasets/reanalysis-era5-single-levels-monthly-means?tab=overview. ERA5 hourly data at the pressure level are available at https://cds.climate.copernicus.eu/datasets/reanalysis-era5-pressure-levels?tab=overview. GPCP precipitation data are available at https://psl.noaa.gov/data/gridded/data.gpcp.html. NOAA snow cover extent data are available at https://www.ncei.noaa.gov/products/climate-data-records/snow-cover-extent. The CESM outputs are available at https://doi.org/10.5281/zenodo.16789206.

Code availability

The codes for CESM experiments, data processing, and plotting are available at https://doi.org/10.5281/zenodo.16789206.

Received: 7 October 2024; Accepted: 6 October 2025; Published online: 19 November 2025

References

- Qiu, J. China: The third pole. Nature 454, 393–396 (2008).
- Yao, T. et al. Recent third pole's rapid warming accompanies cryospheric melt and water cycle intensification and interactions between monsoon and environment: multidisciplinary approach with observations, modeling, and analysis. *Bull. Amer. Meteor. Soc.* 100, 423–444 (2019).
- Huang, J. et al. Global climate impacts of land-surface and atmospheric processes over the Tibetan Plateau. Rev. Geophys. 61, e2022RG000771 (2023).
- An, Z. et al. Evolution of Asian monsoons and phased uplift of the Himalaya–Tibetan Plateau since Late Miocene times. *Nature* 411, 62–66 (2001).
- Kitoh, A. Effects of mountain uplift on East Asian summer climate investigated by a coupled atmosphere—ocean GCM. J. Clim. 17, 783–802 (2004).
- Wu, G. et al. The influence of mechanical and thermal forcing by the Tibetan Plateau on Asian climate. J. Hydrometeor. 8, 770–789 (2007).
- Wang, B. et al. Tibetan Plateau warming and precipitation changes in East Asia. Geophys. Res. Lett. 35, L14702 (2008).
- Held, I. & Ting, M. Orographic versus thermal forcing of stationary waves: the importance of the mean low-level wind. *J. Atmos. Sci.* 47, 495–500 (1990).

- Xie, Y. et al. Oceanic repeaters boost the global climatic impact of the Tibetan Plateau. Sci. Bull. 68, 2225–2235 (2023).
- Liu, Y. et al. Land–atmosphere–ocean coupling associated with the Tibetan Plateau and its climate impacts. Natl. Sci. Rev. 7, 534–552 (2020).
- 11. Zhao, P. et al. Global climate effects of summer Tibetan Plateau. *Sci. Bull.* **64**. 1–3 (2019).
- 12. Immerzeel, W. et al. Importance and vulnerability of the world's water towers. *Nature* **577**, 364–369 (2020).
- 13. Yao, T. et al. Reflections and future strategies for Third Pole environment. *Nat. Rev. Earth Environ.* **3**, 608–610 (2022).
- 14. Duan, A. & Xiao, Z. Does the climate warming hiatus exist over the Tibetan Plateau?. Sci. Rep. 5, 13711 (2015).
- You, Q. et al. Warming amplification over the Arctic Pole and Third Pole: Trends, mechanisms and consequences. *Earth Sci. Rev.* 217, 103625 (2021).
- 16. Tang, S. et al. Regional and tele-connected impacts of the Tibetan Plateau surface darkening. *Nat. Commun.* **14**, 32 (2023).
- Xie, Y. et al. Enhanced Asian warming increases Arctic amplification. Environ. Res. Lett. 18, 034041 (2023).
- Lutsko, N., Baldwin, J. & Cronin, T. The impact of large-scale orography on northern hemisphere winter synoptic temperature variability. J. Clim. 32, 5799–5814 (2019).
- Schär, C. et al. The role of increasing temperature variability in European summer heatwaves. *Nature* 427, 332–336 (2004).
- Tamarin-Brodsky, T. et al. Changes in Northern Hemisphere temperature variability shaped by regional warming patterns. *Nat. Geosci.* 13, 414–421 (2020).
- Baldwin, J., Vecchi, G. & Bordoni, S. The direct and ocean-mediated influence of Asian orography on tropical precipitation and cyclones. *Clim. Dyn.* 53, 805–824 (2019).
- Xu, J. et al. Increasing tropical cyclone intensity in the western North Pacific partly driven by warming Tibetan Plateau. *Nat. Commun.* 15, 310 (2024).
- Wu, G. et al. PV-Q perspective of cyclogenesis and vertical velocity development downstream of the Tibetan Plateau. *J. Geophys. Res. Atmos.* 125, e2019JD030912 (2020).
- Ma, T. et al. Abnormal warm sea-surface temperature in the Indian Ocean, active potential vorticity over the Tibetan Plateau, and severe flooding along the Yangtze River in summer 2020. Quart. J. Roy. Meteor. Soc. 148, 1001–1019 (2022).
- Wu, Z. et al. Can the Tibetan Plateau snow cover influence the interannual variations of Eurasian heat wave frequency?. Clim. Dyn. 46, 3405–3417 (2016).
- Schneider, T., Bischoff, T. & Płotka, H. Physics of changes in synoptic midlatitude temperature variability. J. Clim. 28, 2312–2331 (2015).
- Pelly, L. & Hoskins, B. A New Perspective on Blocking. *J. Atmos. Sci.* 60, 743–755 (2003).
- Hoskins, B. & Hodges, K. The Annual Cycle of Northern Hemisphere Storm Tracks. Part II: Regional Detail. J. Clim. 32, 1761–1775 (2019).
- 29. Su, Z. et al. Impact of the Tibetan Plateau on global high-frequency temperature variability. *J. Clim.* **37**, 4347–4365 (2024).
- Zhou, T. et al. GMMIP (v1.0) contribution to CMIP6: global monsoons model inter-comparison project. Geosci. Model Dev. 9, 3589–3604 (2016).
- Eyring, V. et al. Overview of the Coupled Model Intercomparison Project Phase 6 (CMIP6) experimental design and organization. Geosci. Model Dev. 9, 1937–1958 (2016).
- 32. Danabasoglu, G. et al. The community Earth system model version 2 (CESM2). *J. Adv. Model. Earth. Syst.* **12**, e2019MS001916 (2020).
- 33. Yang, H. et al. The role of mountains in shaping the global meridional overturning circulation. *Nat. Commun.* **15**, 2602 (2024).
- Matthews, T. et al. Latent heat must be visible in climate communications. WIREs Clim. Change 13, e779 (2022).
- Song, F. et al. Trends in surface equivalent potential temperature: A
 more comprehensive metric for global warming and weather
 extremes. *Proc. Natl Acad. Sci. USA* 119, e2117832119 (2022).

- Röthlisberger, M. & Papritz, L. Quantifying the physical processes leading to atmospheric hot extremes at a global scale. *Nat. Geosci.* 16, 210–216 (2023).
- Xie, Y. et al. A potential vorticity budget view of the atmospheric circulation climatology over the Tibetan Plateau. *Int. J. Climatol.* 43, 2031–2049 (2023).
- Xie, Y., Nie, H. & He, Y. Extratropical climate change during periods before and after an Arctic ice-free summer. *Earth's Future* 10, e2022EF002881.
- Shepherd, T. Effects of a warming Arctic. Science 353, 989–990 (2016).
- Yanai, M., Li, C. & Song, Z. Seasonal heating of the Tibetan Plateau and its effects on the evolution of the Asian summer monsoon. *J. Meteorol. Soc. Japan* 70, 319–351 (1992).
- Hoskins, B. & Valdes, P. On the existence of storm-tracks. *J. Atmos. Sci.* 47, 1854–1864 (1990).
- 42. Yang, H. et al. Portraying the impact of the Tibetan Plateau on global climate. *J. Clim.* **33**, 3565–3583 (2020).
- Takaya, K. & Nakamura, H. A formulation of a phase-independent wave-activity flux for stationary and migratory quasigeostrophic eddies on a zonally varying basic flow. J. Atmos. Sci. 58, 608–627 (2001).
- 44. Yang, S. & Wang, Z. Air-sea interactions amplify the global climate effects of the Tibetan Plateau. *Sci. Bull.* **68**, 2689–2690 (2023).
- 45. Wernli, H. & Gray, L. The importance of diabatic processes for the dynamics of synoptic-scale extratropical weather systems—a review. *Weather Clim. Dynam.* **5**, 1299–1408 (2024).
- He, B. et al. The role of air–sea interactions in regulating the thermal effect of the Tibetan–Iranian Plateau on the Asian summer monsoon. *Clim. Dyn.* 52, 4227–4245 (2019).
- Xue, Y. et al. Spring land temperature in Tibetan Plateau and globalscale summer precipitation—initialization and improved prediction. Bull. Amer. Meteor. Soc. 103, E2756–E2767 (2022).
- Liu, S. et al. Near-global atmospheric responses to observed springtime Tibetan Plateau snow anomalies. *J. Clim.* 33, 1691–1706 (2020).
- IPCC. In Climate Change 2021: The Physical Science Basis.
 Contribution of Working Group I to the Sixth Assessment Report of the Intergovernmental Panel on Climate Change (eds Masson-Delmotte V. et al.) 3–32 (Cambridge University Press) (2021).
- Zhang, Q. et al. Oceanic climate changes threaten the sustainability of Asia's water tower. Nature 615, 87–93 (2023).
- Li, F. et al. Arctic sea-ice loss intensifies aerosol transport to the Tibetan Plateau. Nat. Clim. Change 10, 1037–1044 (2020).
- Ma, Y. et al. Dataset of spatially extensive long-term quality-assured land-atmosphere interactions over the Tibetan Plateau. *Earth Syst.* Sci. Data 16, 3017–3043 (2024).
- Yang et al. Cross-sectional rainfall observation on the central-western Tibetan Plateau in the warm season: system design and preliminary results. Sci. China Earth Sci. 66, 1015–1030 (2023).
- 54. Orsolini, Y. et al. Evaluation of snow depth and snow cover over the Tibetan Plateau in global reanalyses using in situ and satellite remote sensing observations. *Cryosphere* **13**, 2221–2239 (2019).
- Zou, H. et al. Validation and application of reanalysis temperature data over the Tibetan Plateau. Acta. Meteorol. Sin. 28, 139–149 (2014).
- 56. Lalande, M. et al. Climate change in the High Mountain Asia in CMIP6. Earth Syst. Dyn. 12, 1061–1098 (2021).
- Chen, X., Liu, Y. & Wu, G. Understanding the surface temperature cold bias in CMIP5 AGCMs over the Tibetan Plateau. Adv. Atmos. Sci. 34, 1447–1460 (2017).
- Hersbach, H. et al. The ERA5 global reanalysis. Quart. J. Roy. Meteor. Soc. 146, 1999–2049 (2020).
- Adler, R. et al. The version 2 global precipitation climatology project (GPCP) monthly precipitation analysis (1979-present). *J. Hydrometeorol.* 4, 1147–1167 (2003).

- Robinson, A. & Estilow, W. NOAA CDR Program: NOAA Climate Data Record (CDR) of Northern Hemisphere (NH) Snow Cover Extent (SCE), Version 1. NOAA National Centers for Environmental Information, https://doi.org/10.7289/V5N014G9 (2012).
- Xie, Y., Huang, J. & Wu, G. Data and code for the paper titled "Changing Northern Hemisphere Weather Linked to Warming Amplification in High Mountain Asia. Zenodo https://doi.org/10.5281/ zenodo.16789206 (2025).
- Yanai, M., Esbensen, S. & Chu, J. Determination of bulk properties of tropical cloud clusters from large-scale heat and moisture budgets. *J. Atmos. Sci.* 30, 611–627 (1973).
- Albornoz, C. et al. Review of atmospheric stability estimations for wind power applications. *Renew. Sust. Energ. Rev.* 163, 112505 (2022).
- The NCAR Command Language (Version 6.6.2) [Software]. Boulder, Colorado: UCAR/NCAR/CISL/TDD, https://doi.org/10.5065/ D6WD3XH5 (2019).
- 65. Benjamini, Y. & Hochberg, Y. Controlling the false discovery rate: A practical and powerful approach to multiple testing. *J. R. Stat. Soc.: Series B* **57**, 289–300 (1995).
- 66. Duchon, C. Lanczos filtering in one and two dimensions. *J. Climatol. Appl. Meteorol.* **18**, 1016–1022 (1979).

Acknowledgements

The authors thank Laurent Li, Martin Menegoz, and the anonymous reviewers for their constructive comments. We thank ECMWF and NOAA for making their data available. We thank the CESM Working Groups NCAR/ UCAR for providing the CESM, version 2.1.3. This work was supported by the National Key R&D Program of China (2023YFF0806700) and the Fundamental Research Funds for the Central Universities (Izujbky-2025-idzx01).

Author contributions

Yongkun Xie: Conceptualized the study, designed the research proposal, developed the technical routes, performed the numerical simulations, and processed and plotted the data. Jianping Huang: Conceptualized the study, designed the research proposal, and developed the technical routes. Guoxiong Wu: Conceptualized the study and designed the research proposal. Jiaqin Mi: Contributed to results analysis, manuscript writing, and revision at all stages. Yimin Liu: Contributed to results analysis, manuscript writing, and revision at all stages. Zifan Su: Contributed to results analysis, manuscript writing, and revision at all stages. Yuzhi Liu: Contributed to results analysis, manuscript writing, and revision at all stages. Xiaodan Guan: Contributed to results analysis, manuscript writing, and revision at all stages.

Competing interests

The authors declare no competing interests.

Additional information

Supplementary information The online version contains supplementary material available at https://doi.org/10.1038/s43247-025-02883-0.

Correspondence and requests for materials should be addressed to Jianping Huang or Guoxiong Wu.

Peer review information Communications Earth and Environment thanks Laurent Li, Martin Menegoz and the other, anonymous, reviewer(s) for their contribution to the peer review of this work. Primary Handling Editor: Alireza Bahadori. A peer review file is available.

Reprints and permissions information is available at http://www.nature.com/reprints

Publisher's note Springer Nature remains neutral with regard to jurisdictional claims in published maps and institutional affiliations.

Open Access This article is licensed under a Creative Commons Attribution-NonCommercial-NoDerivatives 4.0 International License, which permits any non-commercial use, sharing, distribution and reproduction in any medium or format, as long as you give appropriate credit to the original author(s) and the source, provide a link to the Creative Commons licence, and indicate if you modified the licensed material. You do not have permission under this licence to share adapted material derived from this article or parts of it. The images or other third party material in this article are included in the article's Creative Commons licence, unless indicated otherwise in a credit line to the material. If material is not included in the article's Creative Commons licence and your intended use is not permitted by statutory regulation or exceeds the permitted use, you will need to obtain permission directly from the copyright holder. To view a copy of this licence, visit https://creativecommons.org/licenses/by-nc-nd/4.0/.

© The Author(s) 2025